Bubble Behavior in Corrugated-Wall Bubbling Fluidized Beds—Experiments and CFD Simulations

A. N. Khan Wardag and F. Larachi
Dept. of Chemical Engineering, Laval University, Québec City, Québec, Canada G1V 0A6

DOI 10.1002/aic.12725
Published online July 27, 2011 in Wiley Online Library (wileyonlinelibrary.com).

A new concept to harness bubble dynamics in bubbling fluidization of Geldart D particles was proposed. Various geometrical declinations of a cold-prototype corrugated-wall bubbling fluidized bed were compared at different flow rates (U_g) to conventional flat-wall fluidized bed using high-speed digital image analysis. Hydrodynamic studies were carried out to appraise the effect of triangular-shaped wall corrugation on incipient fluidization, bubble coalescence (size and frequency), bubble rise velocity, and pressure drop. Bubble size and rise velocity in corrugated-wall beds were appreciably lower, at given U_g/U_{mb}, than in flat-wall beds with equal flow cross-sectional areas and initial bed heights. The decrease (increase) in size (frequency) of bubbles during their rise was sustained by their periodic breakups while protruding through the necks between corrugated plates. Euler-Euler transient full three-dimensional computational fluid dynamic simulations helped shape an understanding of the impact of corrugation geometry on lowering the minimum bubbling fluidization and improving gas distribution. © 2011 American Institute of Chemical Engineers *AIChE J,* 58: 2045–2057, 2012
Keywords: incipient fluidization, bubble size, bubble coalescence and breakup, bubble rise velocity, corrugated-walled bubbling fluidized bed, digital image analysis, Euler-Euler simulations

Introduction

Anticipating shortages in fossil energy supplies over the next decades is mobilizing sustained efforts in industry and academia to develop efficient renewable energy-based technologies. Residual (nonedible) biomass, owing to its carbon-neutral appeal in relieving greenhouse gas emissions, is explored as an alternative energy source to put a restraint on fossil-energy reliance. Gasification technology for biomass conversion is being brought into focus to convert residual biomass into biofuels or bioproducts.[1] However, significant R&D efforts are still required to come up with innovative gasifier designs. Gasification technology must ideally be bestowed with the following traits: auto/allothermal process, nondiluted biosyngas abolishing downstream N_2 separation or upstream O_2 enrichment, thermal coupling via microsegmentation between endothermic and exothermic steps to improve heat exchanges and enhance thermal efficiency, and high yield and heating value of biosyngas. These attributes represent the foremost challenges next-generation biomass steam gasifiers must cope with. With the endeavor of approaching such ideal configuration, Iliuta et al.[2] proposed a reactor concept of allothermal cyclic multicompartment bubbling fluidized beds. Thermochemical conversion of biomass in periodic time and space sequences of steam biomass gasification and char/biomass combustion was envisioned in which combustion compartments cyclically provide heat into an array of interspersed steam gasification compartments (Figure 1). This concept could enhance unit heat integration and thermal efficiency while procuring N_2-free syngas requiring no addition of oxygen (or air) to steam gasification compartments or contact between flue and synthesis gases.

Most of the studies on indirectly heated fluidized-bed gasifiers agreed on the challenging difficulties to achieve allothermicity. These arise mainly because of significant heat losses and poor heat transfer through the walls that separate the combustion and gasification enclosures.[3–5] While the former concern can be resolved via the numbering-up of microsegmentation between the endothermic and exothermic enclosures as illustrated in Figure SI1 (Supporting Information), the latter needs further investigations as it is related to the quality of fluidization. Hence, a further step to move on with such a concept requires information-gathering about cold-prototype hydrodynamic studies to ascertain bubble structure, dynamics and distribution in non-cylindrical bubbling fluidization enclosures consisting of flat or corrugated walls for heat transfer enhancement.

The efficiency of contacting between gas and particles in bubbling fluidized beds is dictated to a large extent by the bubble dynamics which impacts on heat (fluid-particle and/or wall-to-bed) and mass transfers.[6–14] As bubble breakup and coalescence are directly controlling bubble growth and frequency, and rise velocity,[15–21] a bubbling fluidized bed achieving evenly distributed smaller-size bubbles is expected to operate more efficiently.

Several strategies toward improving the efficiency of fluidized beds have targeted renewal of the bubble surface to interchange fluid between bubbles and interstitial gas in the emulsion phase. Various researchers have realized the

Additional Supporting Information may be found in the online version of this article.

Correspondence concerning this article should be addressed to F. Larachi at faical.larachi@gch.ulaval.ca.

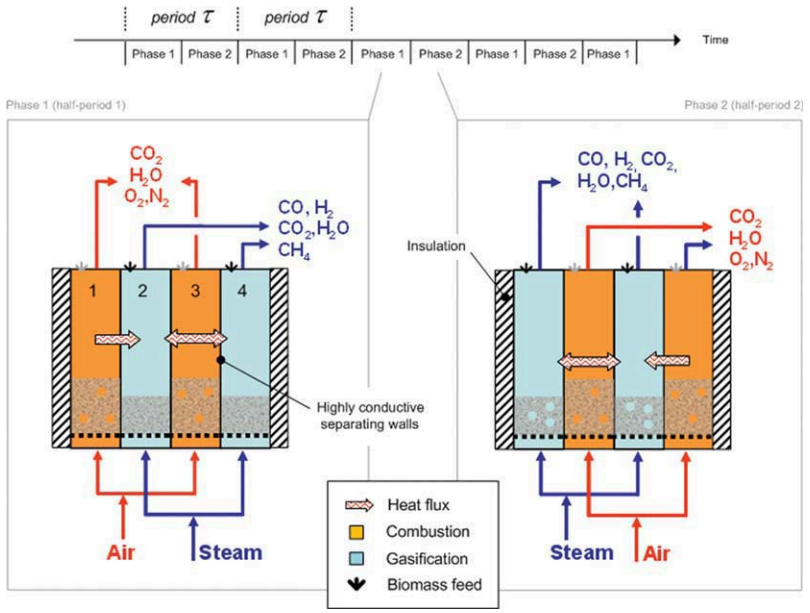

Figure 1. Concept of allothermal cyclic multicompartment fluidized bed for biomass steam gasification.

[Color figure can be viewed in the online issue, which is available at wileyonlinelibrary.com.]

significance of bubbles in gas–solid fluidized beds and used various internals, e.g., baffles, tubes, packings, and inserted bodies, and other configurations to generate evenly distributed smaller bubbles to improve the quality of fluidization. Their main features and inherited limitations have been thoroughly discussed by Jin et al.,[22] the core issues of which are briefly summarized here, along with more recent findings.[23–28] Most transverse baffles in fluidized beds effectively increase gas residence time and reduce solids entrainment. However, this is achieved at the expense of formation at high gas velocities of unwanted gas cushions underneath baffles.[22,27] These dilute gas–solid environments hinder solids motion and favor axial particles segregation and large pressure drops. Horizontal or vertical tube banks have been used for bubble breakup and heat exchange purposes. While vertical arrangements promote better heat transfer, horizontal ones favor bubbles breakup. For an effective use, these have to be placed closer to each other;[29] though closer spacing can promote channeling and gushing both lowering gas–solid exchange and heat transfer performances.[22] Fluidized beds have also been filled with stationary (regular or irregular) and floating packings to break large bubbles for accomplishing even gas distribution. However, when compared with internals-free fluidized beds, their utilization is limited by excessive pressure drop, dead spots, channeling–prompting environment, segregation of particles, and lower effective thermal conductivity.[22] Other innovative designs have recently emerged to reduce bubble sizes and to enhance gas–solid contacting, such as the rotating fluidized bed and its static variant with tangential gas injection,[24,25] and electrically stimulated fluidized beds applying electrical fields on uncharged polarizable particles.[30]

The above survey reveals that the existing geometrical configurations are not easily adaptable to the slim, parallelepipedic and juxtaposed multicompartments depicted in Figure 1 to control bubble structure and dynamics under bubbling fluidization regime as in our proposed setup. Hence, we propose to explore in this study a new concept to harness bubble dynamics in bubbling fluidization by investigating different arrangements of walls with corrugated geometries. To the best of our knowledge, no study is presently available in the literature to address hydrodynamics in corrugated-wall bubbling fluidized beds (CWBFB). In this regard, the proposed research work encompassed cold-prototype experiments to study the effect of corrugations (corrugation angle, interwall clearance, flat versus corrugated, face-to-face opposite or parallel corrugations, horizontal or inclined channel) on minimum bubbling velocity, and bubble size, frequency, and rise velocity. The various geometrical declinations of the cold-prototype CWBFB were compared to the classical flat-wall bubbling fluidized bed (FWBFB) using high-speed digital image analysis (DIA). Euler-Euler transient full three-dimensional (3D) computational fluid dynamic (CFD) simulations were implemented to help understanding the hydrodynamic behavior of CWBFB and to elucidate the origins of fluidization inception as related to corrugation geometrical features.

Experimental

The experiments were carried out in FWBFB and CWBFB made of 2-mm-thick transparent polycarbonate sheets having dimensions as shown in Figure 2a–c and Table 1 (other arrangements are also sketched in Figure SI2, Supporting Information). The seven geometries tested in this work were differentiated using the following nomenclature. F_A and F_B refer to the flat wall geometry for two different initial bed heights, respectively, shallow (F_A, rest height, H_i = 0.15 m) and deep (F_B, rest height, H_i = 0.3 m). Two clearances (C = 0.028 m and 0.038 m, Figure 2a) were tested for the FWBFB. The corrugated-wall geometries were labeled as Cθ_X with C standing for corrugated, θ for the corrugation angle (90° and 120°) and X for distinguishing the horizontal (X = A, B), the opposite inclined (X = C, D), and the parallel inclined (X = E, F) flow channels, Figure 2c. The channels in the opposite and parallel inclined setups were always inclined at 45°. Geometries with X = A, C, and E refer to the shallow beds (H_i = 0.15 m) whereas X = B, D, and F correspond to the deep beds (H_i = 0.3 m). The interwall gap

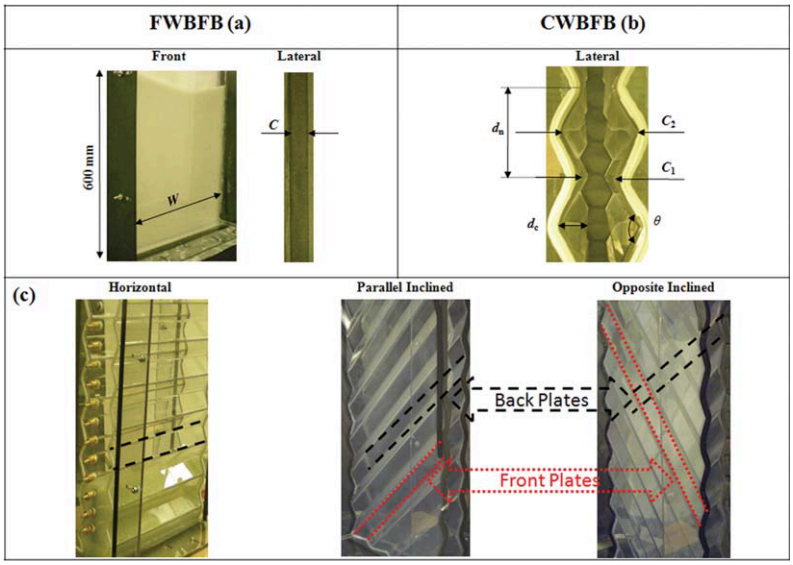

Figure 2. Details of (a) flat wall, (b) corrugated wall, and (c) geometrical arrangements of corrugated wall beds (horizontal, parallel inclined, and opposite inclined).

[Color figure can be viewed in the online issue, which is available at wileyonlinelibrary.com.]

between the viewing corrugated sheets was adjusted to yield a neck clearance, C_1, of 0.015 m (small gap) or 0.025 m (wide gap) for the CWBFB (Figure 2b). A constant corrugation depth, d_c, equal to 0.013 m was kept for both $\theta = 90^\circ$ and 120° corrugations, resulting in neck-to-neck vertical distance, d_n, of 0.03 m for C90_A,B, 0.043 m for C90_C, D, E, F, 0.052 m for C120_A,B, and 0.073 m for C120_C, D, E, F in the fabricated setups (Figure 2b). The average free cross section of the corrugated sheet was estimated from the neck clearance, C_1, the hip clearance, C_2, i.e., the largest passage, and the sheet width, W, as $W(C_1+C_2)/2$ where the width for all the configurations was kept constant at $W = 0.3$ m.

Air was used at ambient conditions as the fluidizing agent. A schematic representation of the experimental setup is given in Figure 3. Geldart D particles were selected as these are difficult to fluidize and show poor quality of fluidization with slugging and spouting in conventional fluidized beds,[30] so the designs of flat- and corrugated-wall beds will address the quality of fluidization. Our working hypothesis is that improvements, if any, brought by corrugated geometries on the fluidization quality of Geldart D particles, *a fortiori*, would translate for particles of other Geldart classes in an as good, if not better, fluidization quality. The selected glass beads had density and diameter of 2500 kg/m^3 and 1.2 mm, respectively. A pressure transmitter having a span of 1 psi was used to register the pressure difference by a data acquisition card (National Instrument, USB-6009). Ten equidistant taps, 0.025 m apart (Figure 3), were used to register the pressure drop readings. The first pressure tap was located 0.055 m above the bed distributor. To estimate bubble properties in both FWBFB and CWBFB, images of the whole bed were taken by a high-speed digital camera (HS-200 TSI, 640 × 480 resolution, software Insight 3G) over 30 s long-time spans at fps = 205 frames per second.

Table 1. Summary of CWBFB and FWBFB Geometries Tested in This Study

CWBFB		H_i (m)	θ (°)	$10^3 \times C_1$ (m)	$10^3 \times d_n$ (m)
C90_A	Horizontal	0.15	90	15, 25	30
C90_B	Horizontal	0.3	90	15, 25	30
C120_A	Horizontal	0.15	120	15, 25	52
C120_B	Horizontal	0.3	120	15, 25	52
C90_C	Opposite inclined	0.15	90	15, 25	43
C90_D	Opposite inclined	0.3	90	15, 25	43
C120_C	Opposite inclined	0.15	120	15, 25	73
C120_D	Opposite inclined	0.3	120	15, 25	73
C90_E	Parallel inclined	0.15	90	15, 25	43
C90_F	Parallel inclined	0.3	90	15, 25	43
C120_E	Parallel inclined	0.15	120	15, 25	73
C120_F	Parallel inclined	0.3	120	15, 25	73

FWBFB		H_i (m)	$10^3 \times C$ (m)
F_A	Flat	0.15	28, 38
F_B	Flat	0.3	28, 38

	Mass of particles (kg)	
Cθ_A, C, E	2.21	2.99
Cθ_B, D, F	4.41	5.99
F_A	2.21 (C = 0.028 m)	2.99 (C = 0.038 m)
F_B	4.41 (C = 0.028 m)	5.99 (C = 0.038 m)

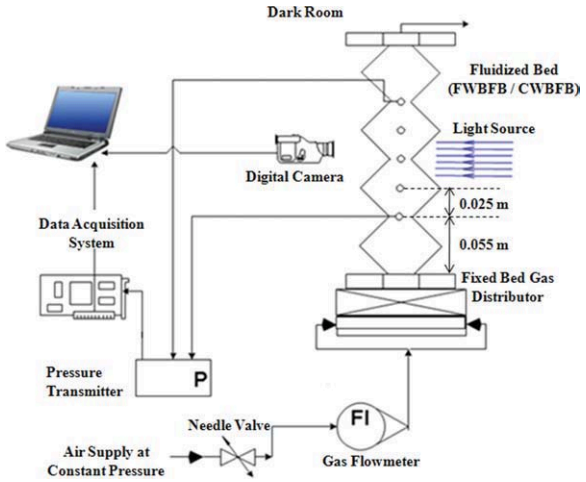

Figure 3. Schematic diagram of experimental setup using digital image analysis technique.

[Color figure can be viewed in the online issue, which is available at wileyonlinelibrary.com.]

The incipient fluidization condition was determined experimentally for each configuration of FWBFB and CWBFB by using pressure drop—gas superficial velocity ($\Delta P - U_g$) plots. For Geldart D particles, an increase in U_g, albeit small, immediately prompts formation of rising bubbles after onset of fluidization in cylindrical or flat-wall fluidized beds, i.e., $U_{mf} \approx U_{mb}$.[8] Gas flow was progressively increased from fixed to fully fluidized bed before it was decreased again to reach the initial rest state. The minimum bubbling velocity was determined by taking the mean of two values obtained from these increasing and decreasing trends. It is designated as U_{mb}^{FW} and U_{mb}^{CW} for the FWBFB and CWBFB, respectively.

Xu et al.[31] estimations indicate that a small portion (15–20%) of steam fed to a fluidized bed gasifier participates in the reaction—the rest serving to maintain fluidization. Air in fluidized bed combustors is apportioned in a similar way to fluidize coal and inert particles.[8] Provided efficiency is not jeopardized, the design of beds operating at lower gas flow rates while ensuring fluidization is preferable. Hence, in this study's context, the degree of fluidization captured via the U_g/U_{mb} ratio would be a better descriptor than the excess gas velocity $U_g - U_{mb}$ when comparing the various bed designs at iso U_g/U_{mb} ratio values.

Note that the values for the FWBFB clearance C were adjusted to be, correspondingly, equal with the average clearance values $(C_1+C_2)/2$ in the CWBFB geometries. In addition, an identical mass of the solids inventory was used for the F_A, Cθ_A, Cθ_C, and Cθ_E geometries to achieve exactly the same bed heights at rest, $H_i = 0.15$ m (Table 1). A similar care was used in packing the beds for the F_B, Cθ_B, Cθ_D, and Cθ_F geometries to yield a matching height, $H_i = 0.3$ m. Constraining the values of the clearances enabled comparison between flat and corrugated beds under equal average superficial velocities and U_g/U_{mb} ratios, whereas forcing equal rest bed heights for flat and corrugated enclosures allowed assessing the gas-particle frictional behavior (same number of solid particles in vessels) as affected by the constraining wall tortuosity, especially near the onset of incipient fluidization.

Using a DIA, images were captured from the widest front side of the bed while the bed backside was exposed to a powerful light source (2 kW total lighting power). The field of view interrogated by the camera was 0.3 m in width and 0.27 m and 0.12 m in height for the deep and shallow options, respectively. The first 0.03 m above the distributor was excluded because of fabrication constraints. Then a series of image processing steps were carried out which used pixel intensity to discriminate between bubble and emulsion phases.[32–34] Figure SI3 (Supporting Information) shows the workflow algorithm used to estimate bubble properties (bubble sizes, velocity, and frequency). Based on this algorithm, a computer program was written in MATLAB. The accuracy of image analysis method was tested by measuring calibrated circular, triangular, and rectangular transparent discs having areas from 177 to 11,304 mm^2. These phantoms were placed at various locations in the flat and corrugated beds. In particular, to check for the optical bias resulting from the corrugated geometries, the phantoms were located at both necks and hips. Examples of calibrations for flat (F), 90° (C90), and 120° (C120) corrugated walls using circular and rectangular shaped disks of various sizes are shown in Figure SI4 (Supporting Information). This figure is a parity plot in which the actual phantoms' projected areas are compared to those reconstructed from our image analysis procedure. It can be concluded that the bubble geometry will be properly captured by our procedure.

All the experiments were carried out at 1.1, 1.25, 1.4, and 1.55 times the U_g to achieve incipient fluidization conditions, i.e., at U_{mb}, for the two different initial bed heights. U_g in the case of CWBFB was calculated based on the average cross section of the bed. The experimental setup was placed in a dark room (except a halogen backlight) where the data-acquisition computer was isolated from the experimental setup with the help of a black curtain to minimize the effect of background light.

Bubble size evolutions were expressed as area-weighted mean bubble diameters instead of the arithmetic-mean or equivalent-diameter from mean area.[35] The first step of image postprocessing consisted in determining the surface area and centroid of each bubble. A bubble was associated with a given elevation when the bubble centroid coincides with the respective vertical position, regardless of lateral position. Up to 900 bubble occurrences were counted at a given elevation over a period of 30 s. The bubble frequency, f_B, at a particular elevation was calculated by dividing the total number of bubbles by 30 s. In a subsequent step, the area weighted mean bubble diameter, D_b, was estimated at each elevation from the ith bubble equivalent diameter, D_i, and surface area, A_i, defined as:

$$D_i = \sqrt{\frac{4A_i}{\pi}} \tag{1}$$

$$D_b = \frac{\sum A_i D_i}{\sum A_i} \tag{2}$$

A bubble rise velocity, U_b, was calculated with respect to the centroid vertical displacement, δ_c, between two consecutive images:

$$U_b = \frac{\delta_C}{\text{fps}^{-1} + \tau_e} \tag{3}$$

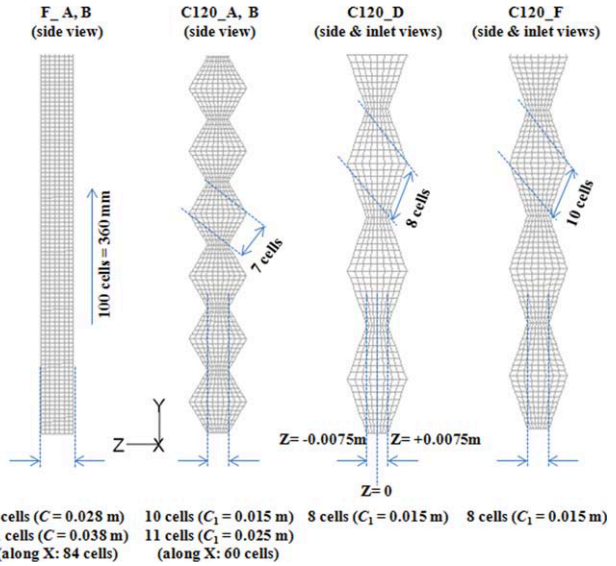

Figure 4. Examples of GAMBIT-generated grid structure for CFD simulations of FWBFB and CWBFB (side and inlet views).

[Color figure can be viewed in the online issue, which is available at wileyonlinelibrary.com.]

where τ_e represents the exposure time (= 0.2 ms). Rise velocities accounted for in the statistics involved exclusively those bubbles which retained more or less a constant projected area between two consecutive images so that events resulting from breakup or coalescence in the interim period were voluntarily discarded. Bubbles whose projected areas remained constant within ±10% were selected.

Computational Aspects

Literature studies showed that CFD simulations can be relied upon to estimate minimum fluidization or bubbling velocity in flat or cylindrical-wall fluidized beds using Geldart D particles. Hence, the onset of incipient fluidization was identified from CFD-generated ($\Delta P - U_g$) or (granular temperature $- U_g$) plots, from noting the abrupt changes in simulated pressure drop or particle velocity time series or from analysis of solids granular temperature.[36–40]

In this work, Euler-Euler full 3D unsteady CFD simulations were carried out to predict the effect of corrugation on minimum bubbling velocity with the aid of FLUENT 6.3.26. Parallel processing on a core-2-Duo CPU associating eight processors was used to perform the simulations. Examples of grid structures of FWBFB and CWBFB generated with GAMBIT are shown in Figure 4 with mesh extrusion conducted along X-direction (vessel width, X ε [0,W]). A comprehensive grid-independence study was also performed by considering various cell sizes as summarized in Table 2.

Simulations were performed with the 3D pressure-based solver in a second-order implicit unsteady formulation and gradients were estimated by the Green-Gauss cell based method. Momentum balance and granular temperature equations were solved using third-order *MUSCL* discretization scheme, and volume fraction using Quick scheme. Pressure–velocity coupling was made by the phase coupled SIMPLE algorithm. All the simulations used a small value of underrelaxation factors for pressure, momentum, volume fraction, and granular temperature in the first few seconds, which were then increased to 0.4 for pressure and momentum and to 0.2–0.3 for volume fraction and granular temperature. Convergence was assumed for each time step as all residuals fell below 10^{-3}.

Air was the continuous primary phase, while solid particles were the secondary discrete phase. At inlet the mass flowrate of continuous phase (air) was used as boundary condition with a range from 0.003 to 0.023 kg/s and a volume fraction of one. Particle velocities (and solids volume fraction) were set to zero at the inlet. The pressure boundary condition at bed outlet was assigned the atmospheric pressure (pressure outlet). The bed walls were treated as no-slip for gas and free-slip for solids phase with granular temperature flux equal zero. Initially, both phases were assigned zero velocities in all directions. Granular temperature and bed solids volume fraction were initialized with 10^{-10} m^2s^{-2} and the measured value of 0.62, respectively. A value of 10^{-6} for solids volume fraction was used in the free board region to achieve convergence during numerical simulations.

Table SI1 (Supporting information) summarizes the two-fluid Euler-Euler conservation equations implemented in Fluent. A value of the coefficient of restitution for particle collisions equal to 0.93 was used to estimate the solids pressure and the solids stress–strain tensor components.[41] The Gidaspow model for granular viscosity and conductivity, the Lun et al. model for granular bulk viscosity, solids pressure, and radial distribution were selected to estimate the secondary phase properties, such as, granular temperature.[41]

Initially, a time step of 10^{-5} s was used and then was gradually increased to 10^{-4} s. Time-averaged results were obtained over periods 25–30 times the mean residence time of gas phase in the bed. To achieve representative time averages, the first 10- to 15-s history was not included in the time averaging.

Results and Discussion

Effect of corrugation on minimum bubbling velocity

CWBFB and FWBFB geometries can be mutually compared on the basis of U_g as their average-enclosure cross sections are equal. Gas, injected from the bottom of the corrugated bed, passes upward through a series of converging and diverging sections. Hence, two additional local superficial gas velocities, U_1 and U_2, are also defined by dividing the volumetric flow rate, respectively, by the neck and the hip cross-sectional areas for the corrugated enclosures (Figure 5).

Figure 6 illustrates the evolution of bed pressure drop as a function of superficial gas velocity for F_B (C = 0.028 m) and C120_B (C_1 = 0.015 m) arrangements with equal average cross-sectional areas and rest bed heights. It can be seen that a

Table 2. Grid Independence Study (d_p = 1.2 mm)

Directions	Grid size
X (width)	F_B: $3d_p$ (selected), $4.2d_p$, $5d_p$
	C120_B: $2d_p$, $3.7d_p$ (selected), $5d_p$
	C120_D: $2d_p$, $3.9d_p$ (selected), $5d_p$
	C120_F: $2d_p$, $3.2d_p$ (selected), $5d_p$
Y (vertical)	F_B: $3d_p$ (selected), $4.2d_p$, $5d_p$
	C120_B: $2.7d_p$ (selected), $3.7d_p$
	C120_ D &F: same as X (width)
Z (horizontal)	F_B: $3.3d_p$ (C = 0.028 m)
	C120_B (C_1 = 0.015m): $1.25d_p$ (neck), $3.4d_p$ (hip)
	C120_D&F (C_1 = 0.015m): $1.6d_p$ (neck), $4.3d_p$ (hip)

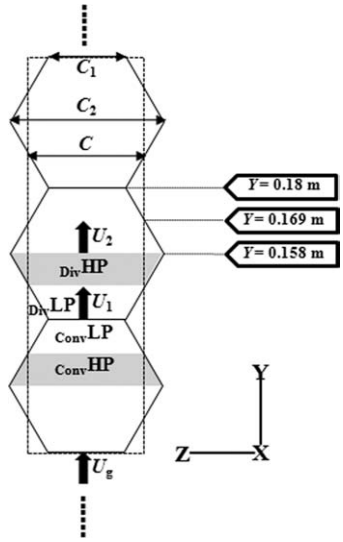

Figure 5. Low-high pressure zones due to the converging-diverging walls and mechanistic interpretation of minimum bubbling fluidization condition in CWBFB (side view).

CWBFB requires a lesser superficial velocity to reach minimum bubbling state than a FWBFB does, i.e., $U_{mb}^{CW} < U_{mb}^{FW}$.

A fixed-bed state in the corrugated geometry can be maintained at a given U_g only if the corresponding U_1 does not exceed the minimum fluidization velocity, U_{mb}^{FW}, of the flat-wall vessel. However, due to wall corrugation, fluidization betides earlier for a given U_g when compared with flat geometry (Figure 6). The differing gas velocity profiles from neck to next hip in the corrugated enclosure prompt large disparities in particle drag forces causing the fixed-bed pressure drop in the corrugated-wall setup to exceed that in the flat-wall one for the same U_g. In view of the increased wallwise tortuosity of the porous medium, CWBFB higher pressure drops in the packed bed state ($U_g < U_{mb}$) is expectable. However, once the incipient fluidization barrier is crossed to enter the bubbling fluidization regime ($U_g \geq U_{mb}$) the pressure drop in the corrugated beds becomes even lower than that accomplished in the flat wall geometry at the same U_g (Figure 6). This state has to

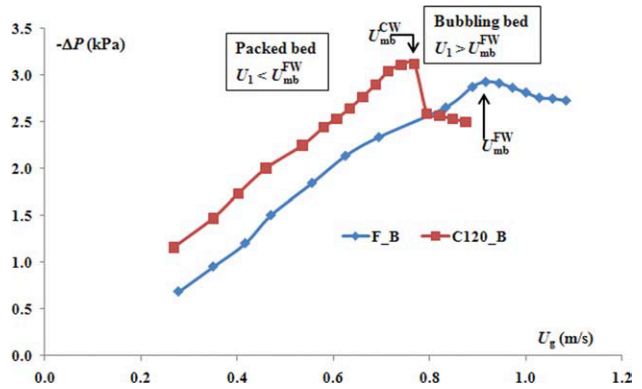

Figure 6. Estimation of incipient bubbling condition by $-\Delta P$ vs. U_g through CWBFB (C120_B, C_1 = 0.015 m) and FWBFB (F_B, C = 0.028 m), based on equal average-enclosure cross section.

In CWBFB, the condition has been achieved at low flow-rate when compared with the FWBFB. [Color figure can be viewed in the online issue, which is available at wileyonlinelibrary.com.]

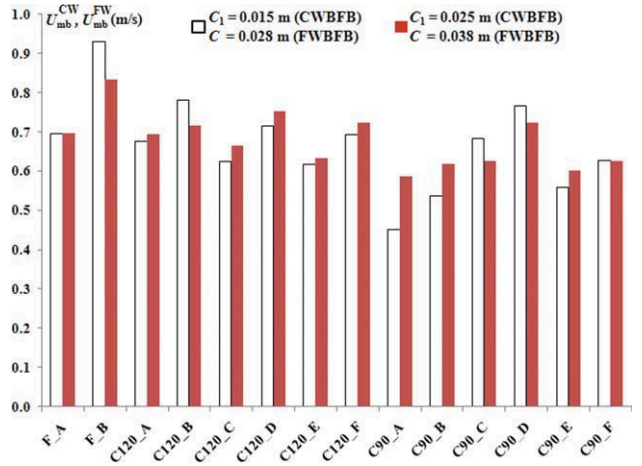

Figure 7. Effect of clearance between the walls and FWBFB and CWBFB arrangements on minimum bubbling velocity.

[Color figure can be viewed in the online issue, which is available at wileyonlinelibrary.com.]

be emphasized as ultimately the application concerns fluidization and not fixed beds. Even if the corrugated-wall fixed bed is more dissipative than its flat-wall analog, the extra dissipation due to corrugation does not exceed 20%. This is not excessive for the gain in pressure dissipation achieved in the fluidization state with the corrugated walls (about −20%).

While increasing U_g, a point is reached where $U_1 \approx U_{mb}^{FW}$ even though U_g for the C120_B geometry is still less than U_{mb}^{FW} (Figure 6). Any further increase in gas flow-rate beyond this point leads to the formation of short-lived bubbles within the converging ($_{Conv}$LP) and diverging ($_{Div}$LP) low pressure zones depicted in Figure 5. However, these leadoff bubbles do not bear enough momentum to protrude through the adjacent converging ($_{Conv}$HP) and diverging ($_{Div}$HP) high pressure zones (Figure 5). An unstable flow pattern hence arises in CWBFB in which the low-pressure zones, barely agitated by the short-lived bubbles, are trapped between almost motionless high pressure zones. This makes delineation of a minimum fluidization velocity, U_{mf}, in CWBFB geometries venturesome. After further increase in gas flow-rate, bubbles acquire sufficient size/momentum to cross the whole bed lengthwise. When this occurs for the first time, the gas superficial velocity, U_g, is referred to as the minimum bubbling velocity, U_{mb}^{CW} (Figure 6).

These findings regarding the incidence of corrugation on U_{mb} are more or less generalizable for the corrugated configurations studied here, see Figure 7. Additionally, it was found that, unlike U_{mb}^{FW}, U_{mb}^{CW} was less sensitive to initial bed height. Also, at the incipient bubbling point, i.e., $U_g = U_{mb}^{CW}$, the neck-based velocity U_1 was always greater than U_{mb}^{FW}, see Figure SI5 (Supporting Information); however, the hip-based velocity, U_2, never exceeded U_{mb}^{FW} (results not shown).

The percent decrease in U_g to achieve minimum bubbling conditions was 22% (C120_B, C_1 = 0.015 m) and 43% (C90_B, C_1 = 0.015 m) with respect to F_B (C = 0.028 m), and 6% (C120_B, C_1 = 0.025 m) and 26% (C90_B, C_1 = 0.025 m) with respect to F_B (C = 0.038 m), respectively. Thus, the narrower the neck the stronger the retreat of minimum bubbling velocity, everything else being kept identical.

Referring to the same vessel geometries as in Figure 6, the CFD-simulated time-averaged fields of gas velocity (colored with gas holdup value), and (F_x, F_y, and F_z) drag force

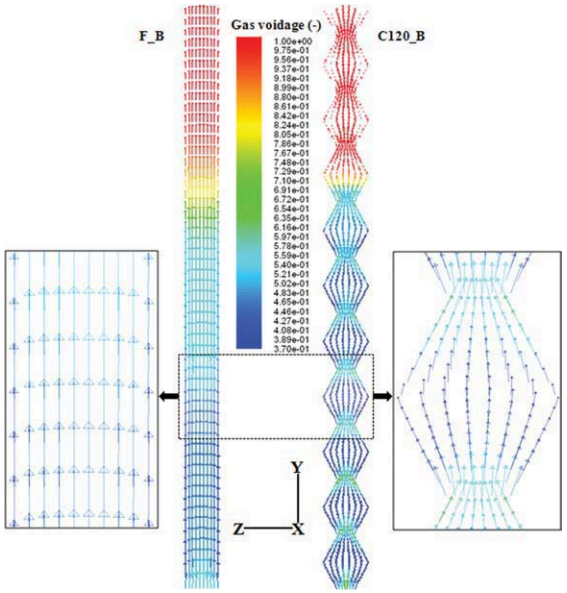

Figure 8. Time-averaged gas velocity field in FWBFB (U_{mb} = 0.93 m/s) and CWBFB (U_{mb} = 0.73 m/s) at $U_g = U_{mb}$, (side view). Insets show enlarged view between Y = 0.135 and 0.18 m, slice taken at X = 0.152 m for F_B (C = 0.028 m) and for C120_B (C_1 = 0.015 m, C_2 = 0.041 m). Contour color parameterized with gas voidage.

[Color figure can be viewed in the online issue, which is available at wileyonlinelibrary.com.]

components at slice position $X = 0.152$ m in FWBFB ($U_g = U_{mb}^{FW} = 0.93$ m/s) and CWBFB ($U_g = U_{mb}^{CW} = 0.73$ m/s) are portrayed, respectively, in Figures 8 and 9. The two insets in Figure 8 are enlarged side views of the velocity fields between elevations $Y = 0.135$ and 0.18 m.

Unlike the FWBFB quasiunidirectional flow, the interstitial gas velocity peaked periodically while gas was funneling through the necks and then sagged at the approach of the CWBFB hips (Figure 8). Gas holdup climaxed at the necks (Figure 8) echoing the periodic pattern of gas velocity. Also, high-gas holdups were more prominent in the low-pressure converging zones, $_{Conv}$LP, than in the diverging ones, $_{Div}$LP, (inset in Figure 8). Both, however, incarnated as many sites propitious to bubble inception as confirmed by visual observations. Despite a lower superficial gas velocity in CWBFB, the particles in the $_{Conv}$LP and $_{Div}$LP zones were experiencing much higher drag forces, especially the y- and z-components, than in FWBFB (Figure 9). Hence, the peaking phenomena in the necks all concur in explicating the precocity of incipient bubbling fluidization due to corrugated walls in accordance with Figures 6 and 7 experimental findings.

The CWBFB and FWBFB gas holdup and granular temperature profiles (Figure 10a,b) were compared at $Y = 0.158$ m and 0.18 m at their respective minimum bubbling velocities. Note that $Y = 0.169$ m is the elevation where the CWBFB is as wide as the FWBFB which demarcates the converging high-pressure and low-pressure zones (Figure 5). The FWBFB gas holdup is bracketed in-between its CWBFB counterparts at the neck ($Y = 0.18$ m) and the hip ($Y = 0.158$ m). This trend is consistent with the fact that the FWBFB is running at higher U_g (= 0.94 m/s) than the CWBFB ($U_g = 0.73$ m/s). It is also sound with regard to the regions prone to bubbles inception as discussed in connection with Figure 8. The CFD simulations also suggest that after crossing the $_{Div}$HP zone ($Y < 0.158$ m), gas builds up near the walls more than at the centerline where the $_{Conv}$LP zone begins ($Y = 0.169$ m). Though the hip plane is less prone to particle fluctuating movements than at the FWBFB corresponding height, particle velocity fluctuations intensify toward the neck plane (Figure 10b). These fluctuations in the $_{Conv}$LP area ($0.169 \leq Y \leq 0.18$) even exceed their FWBFB counterparts. In addition, it is where the gas holdup tends to accumulate the most, i.e., around neck centerline (Figure 10a), that the strongest fluctuating particles motion occurs (Figure 10b). Below $Y = 0.158$ m, the main motion of particles in the $_{Div}$LP and $_{Div}$HP would be due to displacements by the nose of uprising bubbles, tantamount to a forced drift motion. After repositioning and collection of gas flow in the $_{Conv}$HP,

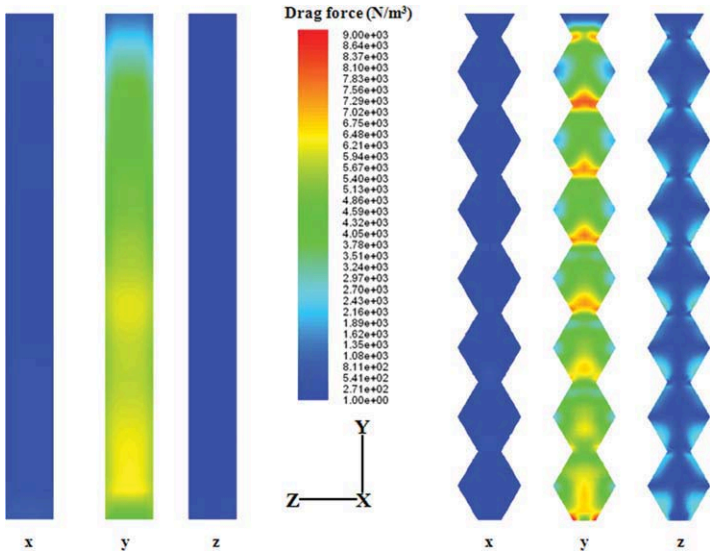

Figure 9. Time-averaged x-, y-, and z-components of drag force for the same conditions as Figure 8 (side view). CWBFB drags at necks exceed those achieved with FWBFB causing incipient bubbling to occur at lower gas flow rate.

[Color figure can be viewed in the online issue, which is available at wileyonlinelibrary.com.]

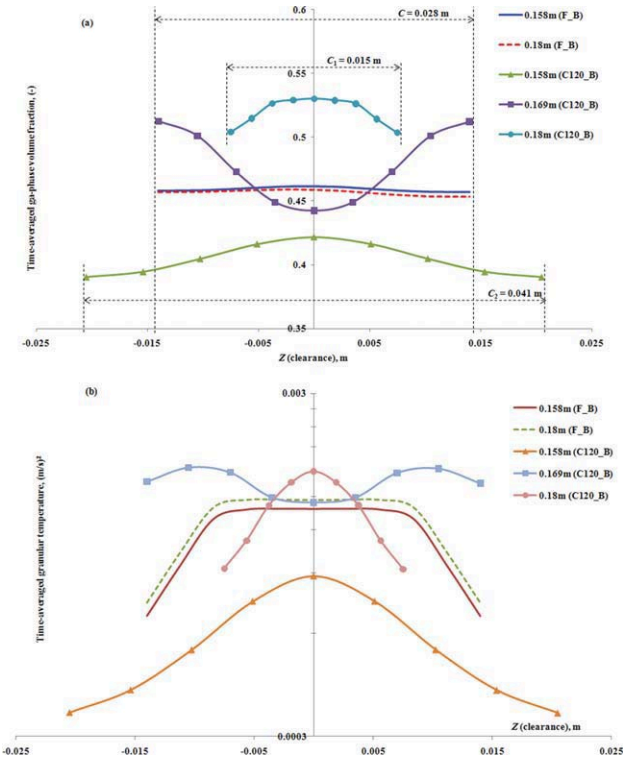

Figure 10. Representative horizontal profiles (side view) of (a) gas volume fraction and (b) granular temperature taken from Figure 8 simulation at vertical positions Y = 0.158, 0.169, and 0.180 m (see Figure 5).

[Color figure can be viewed in the online issue, which is available at wileyonlinelibrary.com.]

the higher gas fraction at $Y = 0.169$ m near the walls causes more particle motion fluctuations than in the center.

CFD simulation reveals that CWBFB offered better gas distribution than FWBFB (Figure 11 and Supporting Information Figure SI6). To compare gas distribution in corrugated beds, Figure. 11a,b contour plots portray the time averaged gas holdup at three bed z-locations (depthwise) in inclined parallel (Figure 11a, C120_F) and inclined opposite (Figure 11b, C120_D) CWBFB at minimum bubbling conditions (see Figure 4 and Supporting Information Figure SI2). The channels' directional bias led to a higher gas voidage at the top right corner in C120_F (Figure 11a) coinciding with uneven bubbles eruption to the freeboard. Experimental observations also confirmed that this parallel configuration brought about a clearly discernible biased gas flow direction. Snapshots in Figure SI7 (Supporting Information) show a few instances of gas–solid fluidization in the parallel-inclined C90_F CWBFB at different superficial gas velocities. The discernible biased gas flow direction was due to the unidirectional corrugations the channels form between two neighboring necks. A stronger bias effect of corrugations on gas flow direction was found in the C90_E and F configurations when compared with C120_E and F configurations. This could be explained by the lesser minimum bubbling velocities required with corrugation angle 90° than with 120°. For instance, the availability of lesser excess gas in C90_F ($U_{mb} = 0.63$ m/s) than in C120_F ($U_{mb} = 0.692$ m/s) led to smaller bubbles in the former than in the latter. Opposite inclined geometries such as C120_C&D and C90_C&D CWBFB, unlike the parallel inclined geometries, eliminated completely the biased flow and led to much better gas distributions (Figure 11b). This time the flowing gas was facing bidirectional channels on either wall of the bed. Therefore, the arrangement and angle of corrugation were very important features of corrugated beds which would affect the quality of fluidization.

It can finally be concluded that CWBFBs offer an advantage with respect to flat-wall beds as the former require lesser gas flow-rates to achieve minimum bubbling conditions, though at the expense of a higher bed pressure drop. CFD simulations identified the necks in CWBFB as being responsible for prompting minimum bubbling fluidization at lower superficial velocity when compared with FWBFB. This behavior was corroborated via the peaking gas holdup, granular temperature, and vertical drag force component at the neck plane of the corrugated walls.

Effect of corrugation on bubble distribution and size

A trajectography analysis of bubbles displacements in flat-wall versus corrugated-wall vessels was performed by plotting the time evolution of bubble centroids tracked over 30 s history as illustrated from the vessels front views in Figure 12a–e and Supporting Information Figure SI8(a,b). In these figures, each case refers to $U_g = 1.4U_{mb}$. These trajectories look like streaks, especially discernible for F_B vessel (Figure 12a), and conform to the life-time each captured bubble resides within the view field.

Bubbles in FWBFB propagate predominantly according to a (short-circuiting) vertical pattern (Figure 12a) while being distributed over the whole bed. However, the parallel horizontal corrugations C120_B (Figure 12b) and C90_B (Figure 12c) induce a peculiar pattern with densification of bubble events along the horizontal necks. In the case of C90_B, the bubbles mainly traveled in the central region of the bed leaving bubble-lean zones on either side of the bed. Similar behaviors are reproduced with the C120_F (Figure 12d) and C90_F [Supporting Information Figure SI8(a)] parallel inclined corrugations where a unidirectional inclined bubbles flow took place. Finally, the cross flow and zigzag motion of bubbles in the opposite inclined corrugated configurations was observed in C120_D (Figure 12e) and C90_D [Supporting Information Figure SI8(b)] resulting in an improved gas distribution. Necks would increase gas-phase residence time in these latter geometries. The localized crowd effect resulting from the trajectory densifications shown in Figure 12b–e is redolent of a particularly active bubble breakup process. This latter leads to the formation of more bubble off-springs in the necks from the fewer and larger parent bubbles that evolved in the (less-densely populated) interneck spaces. Necks, hence, act as many internal redistributors, virtually impeding escapement of large bubbles and perpetually reforming them into smaller bubbles. This function of necks would support the soaring gas holdups revealed earlier on the basis of CFD simulations.

The vertical profiles of the area-weighted mean diameter of bubbles are shown in Figure 13 for the flat bed F_B ($C = 0.028$ m), the corrugated horizontal (C120_B and C90_B) and the inclined opposite (C120_D and C90_D) CWBFB with $C_1 = 0.015$ m and all operating at $1.4U_{mb}$. The Hilligardt and Werther[17] and the Lim et al.[19] correlations for flat-wall bubble size evolutions are also shown for illustration. The latter correlation appears to describe very well the bubble size evolution corresponding to our flat-bed setup.

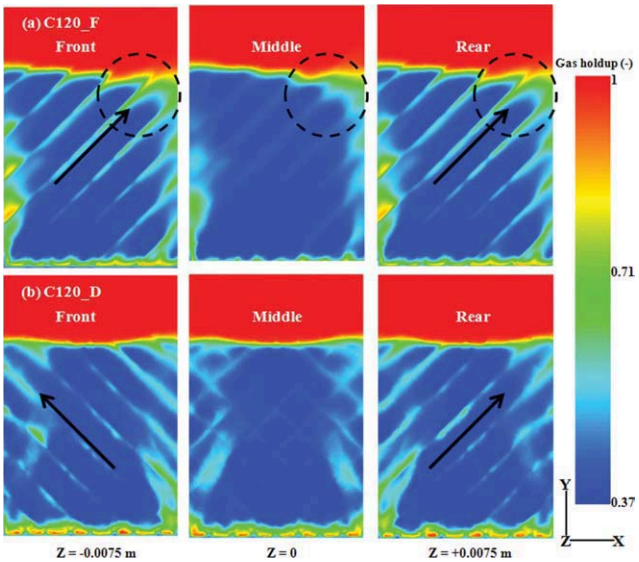

Figure 11. Time-averaged gas holdup contours (XY planes at three *z*-locations) in CWBFB (C_1 = 0.015 m) at $U_g = U_{mb}$ (a) C120_F, (b) C120_D. C120_D offers better gas-distribution when compared with C120_F.

Inclined corrugations in parallel promote bubble eruption at same bed corner (encircled region). [Color figure can be viewed in the online issue, which is available at wileyonlinelibrary.com.]

The periodic oscillations in bubble sizes are noteworthy for all the four corrugated-wall beds (Figure 13); troughs coinciding with necks and apices with hips. Clearly, necks operate as pervading bubble breakup artifices whereas hips allow coalescence to recoup again. In general and as expected, flat-wall fluidized beds offer larger bubbles than the corrugated-wall beds. Exceptions, however, may arise as seen with excursions in bubble size for the C120_B geometry. Bubbles larger than of the flat geometry may periodically overshoot nearby the CWBFB hips presumably because bubble coalescence was more exacerbated. Conversely, the C90_B configuration led to the smallest bubble sizes (Figure 13) where bubble coalescence was presumably retarded the most. However, based on the trajectography results of Figure 12c, this configuration suffers severe channeling toward the center and exhibits poor dispersion for redistributing laterally the smaller bubbles.

Changing θ from 90° to 120° did not reflect as significantly on bubble sizes for the inclined corrugation as in the case of horizontal corrugations (Figure 13). For these latter, $d_n = 0.052$ m for the C120_B unit had a dramatic promoting effect on bubble growth compared to $d_n = 0.03$ m for the C90_B unit. Among the four arrangements of Figure 13, the C90_D geometry represents the best compromise in terms of reduction of bubble size and distribution over the fluidizing medium [Supporting Information Figure SI8(b)]. This can be ascribed to the fact that in opposite inclined CWBFB, at a given elevation Y and while sliding widthwise along X, the C_2/C_1 ratio shrinks and stretches periodically (Figure 2c).

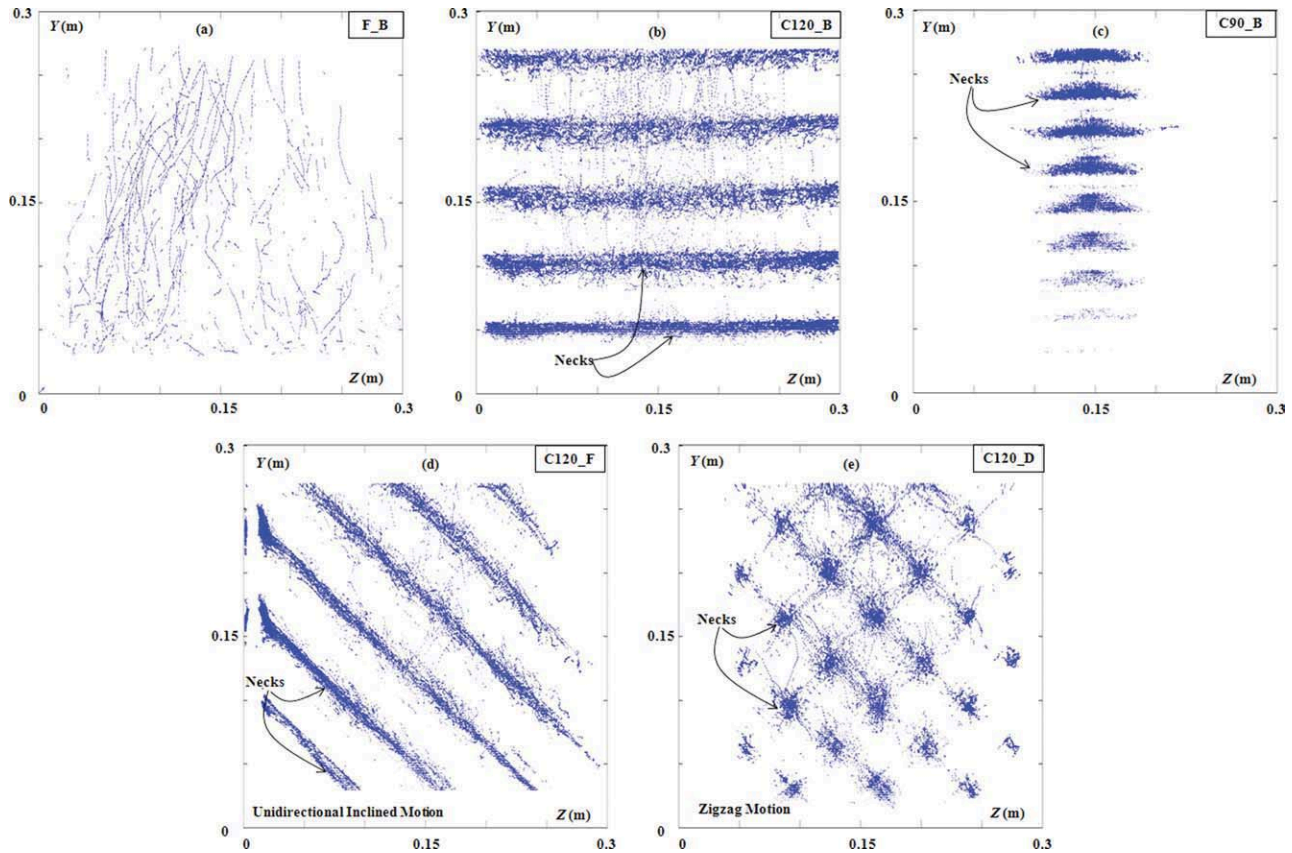

Figure 12. Trajectography of bubble centroids over 30 s in bubbling regime at $U_g = 1.4U_{mb}$, vessel front view (a) F_B (U_{mb} = 0.93 m/s), (b) C120_B (U_{mb} = 0.73 m/s), (c) C90_B (U_{mb} = 0.54 m/s), (d) C120_F (U_{mb} = 0.69 m/s), and (e) C120_D (U_{mb} = 0.71 m/s). (H_i = 0.3 m, and C = 0.028 m or C_1 = 0.015 m).

[Color figure can be viewed in the online issue, which is available at wileyonlinelibrary.com.]

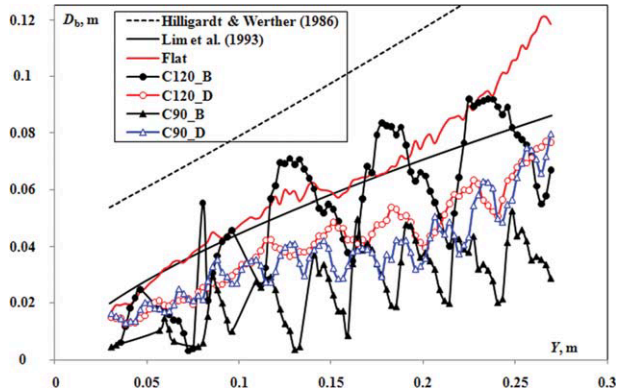

Figure 13. Vertical variation of area-weighted mean bubble diameter in FWBFB (C = 0.028 m) and CWBFB (C_1 = 0.015 m) at $U_g = 1.4U_{mb}$.

CWBFB offer smaller bubbles (except C120_B at hips) due to continuous breakup phenomena at necks and lesser excess gas ($U_g - U_{mb}$) than FWBFB.

This is unlike the horizontal corrugations where this ratio stands still along X axis at any given elevation Y (Figure 2c). Therefore, the inclined opposite CWBFBs are facing simultaneously more of both bubble coalescence and breakup phenomena at a given elevation Y than in the case of the corrugated horizontal CWBFB.

Lateral and vertical coalescence were equally active in flat-wall geometries. Supporting Information Figure SI9(a) shows the location of three rising bubbles (1a, 2a, and 3a) at instants t and $t + \Delta t$ for the flat bed F_B. Bubbles coalesced laterally (1a and 2a yield 1a + 2a) and vertically (bubble 1a + 2a attracts past bubble 3a in its wake) in flat-wall geometries. Horizontal corrugations in C120_A&B and C90_A&B forced bubbles to move vertically straight, leading to small bubbles that were born in the necks to mostly reunite around hips. Bubble coalescence in C120_A&B units was more prominent than in C90_A&B because the neck-to-neck distance, d_n, is about 1.7 times larger (Table 1) which increased the probability of coalescence. The gas superficial velocity was roughly reduced by a ratio C_2/C_1 from neck to hip planes. Hence, bubble growth nearby the hip plane was accomplished through the merger (1d) of slowed-down front bubbles (1c) near the hip with relatively faster bubbles/jets (2c) cropping up from below as shown in Supporting Information Figure SI9(b) for the C120_B unit. Opposite inclined corrugations (C90_D) imparted rising bubbles in zigzag upward motion [Supporting Information Figure SI9(c)]. Small bubbles initially moving upward at time t in one direction at 45° angle changed direction after a while (at $t + \Delta t$). Necks would consequently increase gas-phase residence time in this geometry.

Effect of U_g/U_{mb} *on bubble size, frequency, and rise velocity*

Figure 14a–c depict the effect of U_g/U_{mb} on the vertical profiles of area-weighted mean bubble diameter and bubble frequency in FWBFB (F_B, C = 0.028 m) and CWBFB (C120_D and C90_D, C_1 = 0.015 m) units. An expected increase in bubble size with gas velocity was confirmed regardless of the vessel geometry. In the case of flat-wall geometry, Figure 14a shows that the quality of fluidization begun to deteriorate starting from $U_g = 1.4U_{mb}$ resulting in the formation of slugs, 0.06 to 0.12 m in size (equivalent diameter), particularly in the upper half section of bed (0.15 m $< Y <$ 0.3 m). On the contrary, the quality of fluidization in the (opposite inclined) corrugated vessels improved, and slug formation was repelled up to $1.55U_{mb}$ (smaller bubbles than achieved in F_B unit) and took place closer to the bed disengagement (0.2 mm $< Y <$ 0.3 mm) as exposed by the bubble size profiles in Figure 14b,c. Hence, it may be concluded that CWBFB can exhibit a broader operational range than FWBFB and can be operated up to higher gas flow-rates while avoiding slug formation.

As far as bubble frequency was concerned, an expected decrease in frequency along bed height was obtained at all the flow conditions of the F_B unit (Figure 14a). At the lowest U_g value, bubble frequency barely changed as a function of Y and bubble coalescence was the least. At elevations preceding slug formation, the frequency of bubbles increased with increasing U_g as a result of availability of more excess gas. Ultimately, slugs formed in the bed upper part due to boosted bubble coalescence.

Very peculiar bubble frequency measurements were obtained in the case of CWBFB. The use of CWBFB for given U_g/U_{mb} and elevation contributed to increase bubble frequency by reducing bubble size even if the beds operated at lower excess gas than flat walls. For instance, the excess gas velocity in F_B (U_{mb} = 0.93 m/s) amounted to 0.372 m/s, whereas for C90_D (U_{mb} = 0.766 m/s) it attained about 0.31 m/s, nearly 18% less than in F_B. This is due to the special feature of corrugated walls in opposite inclined walls as discussed in connection with Figure 13 and Supporting Information Figures SI8(b) and SI9(c) above as they offer intermeshed bubble coalescence and breakup phenomena along X directions. Within the same CWBFB, an increase in gas velocity also resulted in increased bubble frequencies. Also, bubble frequency was observed to be more sensitive to gas superficial velocity in the lower-half section of the beds when compared with the upper-half section (Figure 14b,c).

Figure 14b,c also reveal that the oscillatory behavior of bubble frequency and bubble diameter are in "phase opposition"; bubble size is maximum, and bubble frequency is minimum in the hips and bubble size is minimum and bubble frequency is maximum in the necks of the corrugated fluidized beds. It may be possible that bubble size reduction nearby the neck regions presumably could proceed following shrinkage of the large bubbles via local replenishment of the emulsion phase with interstitial gas. This in turn could lead to the formation of small bubbles in the neck regions explaining the surge in frequency of the smaller bubble sizes. This mechanism cannot be ruled out and may be concurrent with the simpler mechanism whereby larger bubbles in the neck regions erode due to the very strong shearing action manifesting there to yield their smaller bubbles offsprings. DIA technique registers and counts rising bubbles (whether deforming their shapes or experiencing coalescence and breakup) through necks and hips. On the basis of this counting, the periodic behavior in bubble frequency data in Figure 14b,c confirms that bubble breakup and coalescence are active.

Figure 15 shows a typical trend of bubble rise velocities along the vertical direction for three bed geometries: FWBFB (F_B, C = 0.028 m) and CWBFB (C120_D and C90_D, C_1 = 0.015 m) units. The inclined trajectories of bubbles, as imposed by the inclined opposite corrugated

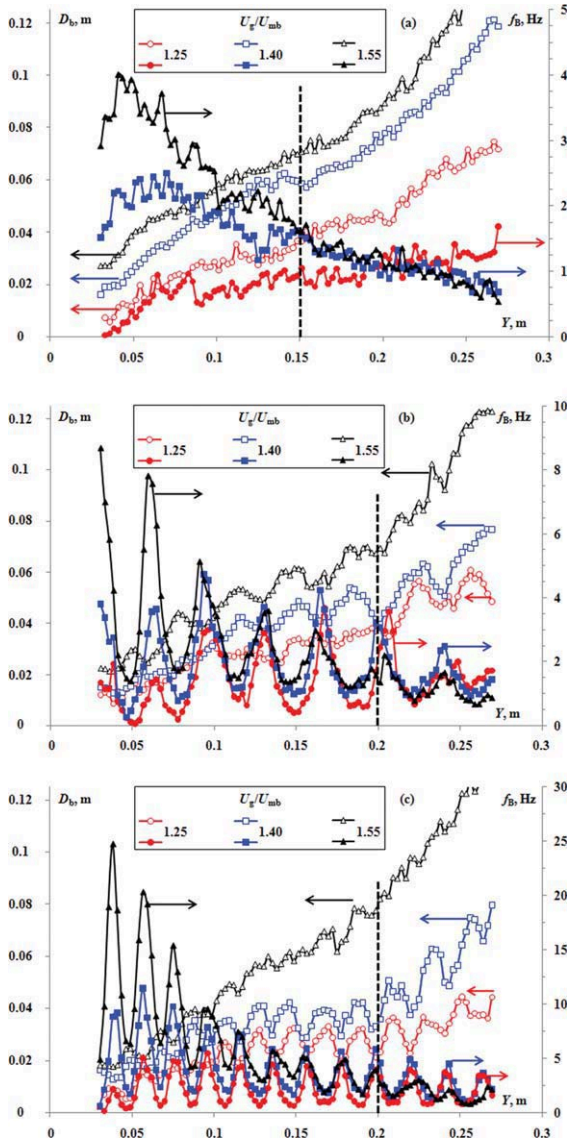

Figure 14. Effect of U_g/U_{mb} ratio on bubble growth and frequency for (a) F_B, (b) C120_D and (c) C90_D fluidized bed units. Slug formation dotted line U_g/U_{mb} = 1.4 (flat wall) and 1.55 (corrugated wall), empty symbol: D_b, filled symbol: f_B.

[Color figure can be viewed in the online issue, which is available at wileyonlinelibrary.com.]

walls, in addition to reducing bubble sizes, also, correlatively, contributed in decreasing their rise velocity in comparison with a flat-wall geometry.

Conclusions

Gas–solid mixing and heat transfer problems could still demand for new efficient designs of gas–solid fluidized beds. As heat transfer depends on gas–solid mixing, and is directly controlled by bubble sizes and distribution, the current research work focused on improving bubble properties. A new design of CWBFB was proposed in a quest for better fluidization quality with smaller bubbles. It was observed that CWBFB effectively reduced the gas flow-rate required to achieve incipient fluidization when compared with flat-wall fluidized beds with equal cross-sectional area for the same gas–solid system. This could economize the process by lowering the demand of extra unreacting gas (e.g., air in combustion and steam in gasification unit) required to fluidize the particles. Experimental results obtained at U_g equal 1.1, 1.25, 1.4, and 1.55 times the minimum bubbling velocities for Geldart-D particles indicated that CWBFB decreased sensibly the bubble sizes when compared with the flat-wall setups. This was attributed to the less excess gas ($U_g - U_{mb}^{CW}$) and continuous bubbles breakup phenomena at the necks of CWBFB. A continuous increase/decrease in bubble growth was obtained with decreasing/ increasing trends in bubbles frequency. Bubble rise velocity mirrored those trends. Slugging was repelled up to higher flow-rates in CWBFB enlarging their operational range with better quality of fluidization. While comparing different configurations of corrugations in CWBFB, it was concluded that opposite inclined corrugated beds (C120_C&D and C90_C&D) maintained a right balance between bubble sizes and their spatial distribution. Two neck clearance values (C_1 = 0.015 m and 0.025 m) were tested for a constant corrugation depth in the current study. Image analysis results showed that a better quality of fluidization could be obtained at $C_1 < 0.025$ m. However, increasing C_1 led to bed behaviors closer to those in a flat-wall bed.

Particles circulation and wall-to-bed heat transfer studies in case of corrugated walls are as important as bubble dynamics studies. Currently, study of the former two aspects is under progress and will hopefully be the subject of future communications. Bed visual inspection already revealed that horizontally arranged corrugated walls occasion dead zones in the hip corners. Inclined arrangements, on the contrary, clearly promote a convective downward flow of particles—when these are not circumscribed in the bubble wakes—along the inclined walls which may improve mixing and wall heat transfer. Therefore, corrugation (θ) and inclination (α) angles for the same clearance between walls would play crucial roles in suppressing dead zones. As far as FWBFB are concerned, calming zones are also possible at the extreme ends of beds for high flow rates whereby larger bubbles mainly protrude through the bed central part. Such calming zones are suppressed in the CWBFB owing to a

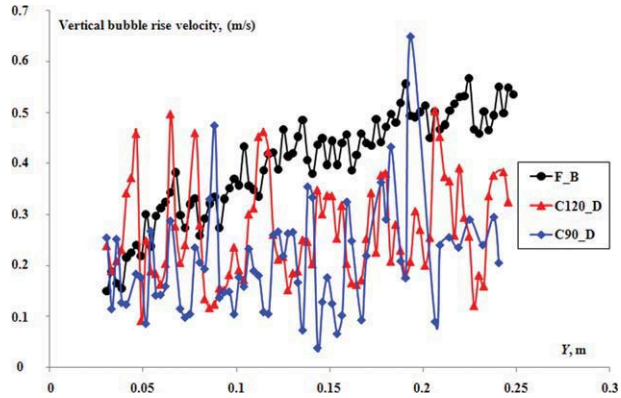

Figure 15. Effect of corrugation on vertical bubble rise velocity at $U_g = 1.4U_{mb}$ for F_B, C120_D and C90_D fluidized bed units: (C_1 = 0.015 m, C = 0.028 m).Fluctuating behavior due to continuous change in bubble size.

[Color figure can be viewed in the online issue, which is available at wileyonlinelibrary.com.]

better gas distribution. CFD simulations validated that CWBFB offer high gas hold up and drag force at necks than FWBFB easing formation of bubbles and achieving earlier incipient fluidization condition. In addition, opposite inclined CWBFB setups offered superior gas distribution than FWBFB.

Finally, to incite comparisons of corrugation over baffles in bubbling fluidization, air cushions in CWBFB did not form with the former. Even if the corrugated-wall fixed bed is more dissipative than its flat-wall analog, the extra dissipation due to corrugation does not exceed 20%. The distance between adjacent layers of baffles is often in the range of 0.4–0.6 m, whereas in CWBFB the neck-to-neck distance (d_n) varies from 0.03 to 0.073 m generating bubbles with sufficient momentum to come across the adjacent hip zones and ultimately the whole bed. Baffles cannot produce bubbles with sufficient momentum at low gas flow rate to cross 0.4–0.6 m high bed sections. Compared to the minimum interbaffle distance of 0.4 m, CWBFB offers five times (C120_D, $d_n = 0.073$ m) and up to nine times (C90_D, $d_n = 0.043$ m) more bubble breakup sites. Our work proposed to explore slim, parallelepipedic and juxtaposed multicompartment gas–solid fluidized beds in which each compartment can work independently easing heat integration; baffles could barely lend themselves to such adaptation.

Acknowledgments

The Natural Sciences and Engineering Research Council of Canada Strategic Grant Program and the Canada Research Chair "Green processes for cleaner and sustainable energy" are gratefully acknowledged for their financial support. One of the authors (ANKW) gratefully acknowledges the Pakistan Institute of Engineering and Applied Sciences for his PhD scholarship. A. Leclerc help in providing some illustrations is appreciated.

Notation

A_i = surface-area of bubble, mm^2
C = clearance between flat plates in FWFB, m = $(C_1 + C_2)/2$
C_1 = neck clearance in CWBFB, m
C_2 = hip clearance in CWBFB, m
D_b = area-weighted mean bubble diameter, m
d_c = corrugation depth, m
D_i = equivalent diameter of bubble, m
d_n = neck-to-neck vertical distance, m
d_p = particle diameter, mm
F_i = i-th component drag force per unit volume, N/m^3
f_B = bubble frequency, Hz
fps = frames per second, Hz
H_i = Initial height of the bed, m
U_1 = gas superficial velocity at C_1, m/s
U_2 = gas superficial velocity at C_2, m/s
U_b = bubble rise velocity, m/s
U_g = gas superficial velocity, m/s
U_{mb} = minimum bubbling velocity in BWFB, m/s
v_i = i-th component interstitial gas velocity, m/s
W = width of fluidized bed, m
ΔP = pressure drop, kPa
X, Y, Z = cartesian coordinates, m

Greek letters

δ_c = bubble centroid vertical displacement between two consecutive images, m
θ = corrugation angle (90° and 120°)
τ_e = exposure time, s

Abbreviations

CWBFB = corrugated-walled bubbling fluidized bed
DIA = digital image analysis technique
FWBFB = flat-wall bubbling fluidized bed

Literature Cited

1. Huber GW, Iborra S, Corma A. Synthesis of transportation fuels from biomass: chemistry, catalysts, and engineering. *Chem Rev*. 2006;106:4044–4098.
2. Iliuta I, Leclerc A, Larachi F. Allothermal steam gasification of biomass in cyclic multi-compartment bubbling fluidized bed gasifier/combustor—new reactor concept. *Bioresource Technol*. 2010; 101:3194–3208.
3. Kunii D. Apparatus for thermally decomposing and gasifying combustible material in a single fluidized reactor, US Patent 4,337,066, 1982.
4. Kunii D. Process and apparatus for gasifying combustible materials, US Patent 4,405,339, 1983.
5. Corella J, Toledo JM, Molina G. A review on dual fluidized-bed biomass gasifiers. *Ind Eng Chem Res*. 2007;46:6831–6839.
6. Ozkaynak T, Chen JC. Emulsion phase residence time and its use in heat transfer models in fluidized beds. *AIChE J*. 1980;26:544–550.
7. Syamlal M, Gidaspow D. Hydrodynamics of fluidization: prediction of wall-to-bed heat transfer coefficients. *AIChE J*. 1985;31:127–135.
8. Kunii D, Levenspiel O. *Fluidization Engineering*, 2nd ed. Newton, MA: Butterworth-Heinemann Series in Chemical Engineering, 1991.
9. Kuipers JA, Prins W, van Swaaij WPM. Numerical calculation of wall-to-bed heat transfer coefficients in gas solid fluidized beds. *AIChE J*. 1992;38:1079–1091.
10. Molerus O, Burschka A, Dietz S. Particle migration at solid surfaces and heat transfer in bubbling fluidized beds-II. Prediction of heat transfer in bubbling fluidized beds. *Chem Eng Sci*. 1995;50:879–885.
11. Chen JC. Surface contact-its significance for multiphase heat transfer: diverse examples. *J Heat Trans–T ASME*. 2003;125:549–566.
12. Solimene R, Marzocchella A, Ragucci R, Salatino P. Laser diagnostics of hydrodynamics and gas-mixing induced by bubble bursting at the surface of gas-fluidized beds. *Chem Eng Sci*. 2007;62:94–108.
13. Shen L, Xiao J, Niklasson F, Johnsson F. Biomass mixing in a fluidized bed biomass gasifier for hydrogen production. *Chem Eng Sci*. 2007;62:636–643.
14. van Ommen RJ, Mudde RF. Measuring the gas-solids distribution in fluidized beds—a review. *Int J Chem React Eng*. 2008;6:R3.
15. Toei R, Matsuno R, Sumitani T, Mori M. Coalescence of bubbles in gas-solid fluidized beds. *Int Chem Eng*. 1968;8:351.
16. Darton RC, La Nauze RD, Davidson JF, Harrison D. Bubble growth due to coalescence in fluidized beds. *Trans IChemE*. 1977;55:274–280.
17. Hilligardt K, Werther J. Local bubble gas hold-up and expansion of gas/solid fluidized beds. *German Chem Eng*. 1986;9:215–221.
18. Yates JG, Ruiz-Martinez RS, Cheesman DJ. Prediction of bubble size in a fluidized bed containing horizontal tubes. *Chem Eng Sci*. 1990;45:1105–1111.
19. Lim KS, Gururajan VS, Agrawal PK. Mixing of homogeneous solid in bubbling fluidized beds: theoretical modeling and experimental investigation using digital image analysis. *Chem Eng Sci*. 1993;48:2251–2265.
20. Fan LS. Summary paper on fluidization and transport phenomena. *Powder Technol*. 1996;88:245–253.
21. Shen L, Johnson F, Leckner B. Digital image analysis of hydrodynamics in two dimensional bubbling fluidized beds. *Chem Eng Sci*. 2004;59:2607–2617.
22. Jin Y, Wei F, Wang Y. *Effect of internal tubes and baffles*. In: Yang WC, editor. *Handbook of Fluidization and Fluid-particle Systems*. New York: Marcel Dekker, 2003, Chapter 7.
23. He YR, Lu HL, Sun QQ, Yang LD, Zhao YH, Gidaspow D, Bouillard J. Hydrodynamics of gas-solid flow around immersed tubes in bubbling fluidized beds. *Powder Technol*. 2004;145:88–105.
24. Nakamura H, Iwasaki T, Watano S. Modeling and measurement of bubble size in a rotating fluidized bed. *AIChE J*. 2007;53:2795–2803.
25. De Wilde J, De Broqueville A. Rotating fluidized bed in a static geometry: experimental proof of concept. *AIChE J*. 2007;53:793–810.
26. Zhang YM, Lu CX, Grace JR, Bi XT, Shi M. Gas back-mixing in a two dimensional baffled turbulent fluidized bed. *Ind Eng Chem Res*. 2008;47:8484–8491.
27. Zhang Y, Grace JR, Bi X, Lu C, Shi M. Effect of louver baffles on hydrodynamics and gas mixing in a fluidized bed of FCC particles. *Chem Eng Sci*. 2009;64:3270–3281.

28. Wormsbecker M, Pugsley T, Tanfara H. Interpretation of the hydrodynamic behaviour in a conical fluidized bed dryer. *Chem Eng Sci*. 2009;64:1739–1746.
29. Yates JG, Ruiz-Martinez RS. Interaction between horizontal tubes and gas bubbles in a fluidized bed. *Chem Eng Commun*. 1987;62:67–78.
30. van Willigen FK, van Ommen JR, van Turnhout J, van den Bleek C. Bubble size reduction in a fluidized bed by electric fields. *Int J Chem React Eng*. 2003;1:A21.
31. Xu G, Murakami T, Suda T, Matsuzawa Y, Tani H. Gasification of coffee grounds in dual fluidized bed: performance evaluation and parametric investigation. *Energy Fuels*. 2006;20:2695–2704.
32. Agarwal PK, Hull AS, Lim KS. *Digital image analysis techniques for the study of bubbling fluidized beds*. In: Chaouki J, Larachi F, Dudukovic MP, editors. *Non-invasive Monitoring of Multiphase Flows*. Amsterdam, The Netherlands: Elsevier Science, 1997, Chapter 12.
33. Busciglio A, Vella G, Micale G, Rizzuti L. Analysis of the bubbling behaviour of 2D gas solid fluidized beds. Part I: digital image analysis technique. *Chem Eng J*. 2008;140:398–413.
34. Laverman JA, Roghair I, van Sint Annaland M, Kuipers H. Investigation into the hydrodynamics of gas-solid fluidized beds using particle image velocimetry coupled with digital image analysis. *Can J Chem Eng*. 2008;86:523–535.
35. Patil DJ, van Sint Annaland M, Kuipers JA. Critical comparison of hydrodynamic models for gas–solid fluidized beds-Part II: freely bubbling gas–solid fluidized beds. *Chem Eng Sci*. 2005;60:73–84.
36. Xu BH, Yu AB. Numerical simulation of the gas-solid flow in a fluidized bed by combining discrete particle method with computational fluid dynamics. *Chem Eng Sci*. 1997;52:2785–2809.
37. Ye M, van der Hoef MA, Kuipers JAM. The effects of particle and gas properties on the fluidization of Geldart A particles. *Chem Eng Sci*. 2005;60:4567–4580.
38. Tan KK, Tan YW, Tey BT, Look KY. On the onset of incipient fluidization. *Powder Technol*. 2008;187:175–180.
39. Bahramian A, Kalbasi M, Olazar M. Influence of boundary conditions on CFD simulation of gas-particle hydrodynamics in a conical fluidized bed unit. *Int J Chem React Eng*. 2009;7:A60.
40. Wang JW, van der Hoef MA, Kuipers JAM. CFD study of the minimum bubbling velocity of Geldart A particles in gas-fluidized beds. *Chem Eng Sci*. 2010;65:3772–3785.
41. Fluent User's Guide, 2006. Lebannon: Fluent Inc.

Manuscript received Nov. 4, 2010, revision received Apr. 18, 2011, and final revision received June 29, 2011.